MECHANISM OF CRACK INITIATION BY THERMAL FATIGUE AND CRACK PROPAGATION IN THE CASE OF HOT ROLLING ROLLS.

A. Dias, J. Giusti, H.-P. Lieurade*

In the case of hot rolling rolls two stages of damage have been studied on two typical steels : the first corresponds to crack initiation by thermal fatigue, the second to crack propagation due to mechanical loads.

A thermal fatigue simulator was then developed, as well as a finite element elastoplastic model, to determine the mechanical solicitations at the roll surface.

The fatigue crack propagation laws were then estimated for each steel.

The results were analysed according to the mechanical and metallurgical parameters of the materials studied.

INTRODUCTION

Hot work rolls suffer in service hard thermal and mechanical conditions producing a thermal fatigue damage. This low-cycle fatigue leads to a superficial honeycomb cracking, figure 1. These cracks grow under rolling mechanical loads and water cooling corrosion can increase the damage. As their size increases the cracks play a harmful effect on the surface quality and geometry of the rolled products and can even lead to the rolls fracture. The present study considers the following stages of damage :

- crack initiation by honeycomb cracking ;
- crack propagation during rolling cycles, due to mechanical efforts,

and compares the behaviour of two typical materials.

The variation of the surface temperature during the rotation of a hot work roll (first finishing stand) are calculated analytically using a thermal model, figure 2. The thermal cycle obtained is reproduced on a thermal fatigue simulator and the results of these experiments are correlated to the thermal and mechanical properties (coefficient of linear expansion, tensile strength, hardness, low-cycle fatigue behaviour and toughness).

The fatigue crack growth rates of the materials are then compared, as well as the resulting surfaces of fracture.

In order to study the material behaviour by a thermomechanical test, a finite element analysis is conducted to estimate the thermomechanical loading at the surface of the roll.

The stress-corrosion tests have been carried out in order to estimate the influence of this parameter on the cracking mechanism.

* Institut de Recherches de la Sidérurgie Française (IRSID)
78105 SAINT GERMAIN EN LAYE CEDEX - France.

Materials and experimental procedure

Materials. The characteristics of the materials tested in this study are presented in table 1.

TABLE 1 - Chemical analysis and heat treatment.

Steel	Chemical Analysis (%)									Heat treatment	Structure
	C	Mn	Si	P	S	Ni	Cr	Mo	V		
A	0.8	0.8	0.4	0.011	0.015	0.7	1.0	0.3	0.03	Hardened and tempered	Bainite
B	1.6	1.3	0.4	0.003	0.013	0.7	1.2	0.3		Normalized and annealed	Perlitic matrix + cementite carbides

Tensile tests. Tensile tests were carried out at different temperatures (between room temperature and 600°C) and strain rates ($\dot{\varepsilon} = 6.7 \times 10^{-4}$ s^{-1} and $\dot{\varepsilon} = 1.2 \times 10^{-1}$ s^{-1}). The specimens were heated in a resistance furnace. For the tests performed at $\dot{\varepsilon} = 1.2 \times 10^{-1}$ s^{-1}, load-displacement signals were recorded using a numerical oscilloscope with buffer memories.

Hardness tests. Hardness tests at elevated temperatures were performed on a testing apparatus developed at IRSID. This machine measures Vickers hardness in vacuum between room temperature and 1000°C.

Low-cycle fatigue tests. Isothermal low-cycle fatigue tests were carried out in a temperature range between room temperature and 600°C. The apparatus consists of an electro-hydraulic, servo-controlled, push-pull type fatigue machine. The strain rate of the triangular waveform strain controlled cycle was of $\dot{\varepsilon} = 4.10^{-3}$ s^{-1}. For strain measurement a longitudinal extensometer was used.

Thermal fatigue simulator tests. A special apparatus for testing thermal fatigue has been developed and built at IRSID (1). The method is based on high frequency heating of the surface of a cylindrical sample, in which the non-heated core material constrains the surface dilatation. The cooling of the specimen is accelerated by an external water-jet cooling. The material is, thus, subjected to thermal and stress cycles similar to those appearing in hot work rolls. The calculated thermal cycles, between room temperature and 600°C, were then applied at the surface of the samples. According to the similar values of thermal conductivity, the radial gradients of steels A and B are closely related.

Fracture mechanics tests. The estimations of K_{Ic} and K_{Iscc} were made in standard conditions.

Fatigue crack growth tests were carried out in air at constant amplitude loading, with an R ratio equal to 0.1 and a frequency of 30 Hz. CT test specimens were employed.

Results

Tensile tests. The results obtained at several temperatures and two strain rates are presented in figures 3a and 3b. The strain rate of $\dot{\varepsilon} = 1.2 \times 10^{-1}$s^{-1} was chosen because it is in the range of strain rate values of the roll surface (contact time coil-roll $\simeq$ 0.1 s).

Hardness tests. Figure 4 shows the hardness data at elevated temperatures. This kind of test is justified by the following reasons :

- hardness is the checking test most often applied in roll manufacture ;
- steel B presenting a brittle behaviour in tension for every temperature, hardness values give an estimation of the compression strength of the material.

Low-cycle fatigue tests at room temperature. Figure 5 shows the total and plastic strain ranges and the steady stress amplitude versus the number of cycles until fracture. Cyclic parameters in Table 2 are compared to tensile characteristics. In the strain range studied these materials show a cyclic strain softening.

TABLE 2 - Mechanical properties.

Steel	$R_{e0,2}$ MPa	Rm MPa	$R'_{e0,2}$ MPa	n'	K' MPa	c	m	m/n'
A	860	1200	660	0,19	2120	1.45×10^{-13}	3.4	18
B	470	500	450	0.26	2100	3.75×10^{-15}	5.5	21

Thermal simulator tests. Each sample was tested between 500 and 5000 thermal cycles. The evolution of crack density was metallographically measured on the middle cross-section of the specimens. This estimation was made for several crack lengths, figures 6a and 6b.

Fatigue crack growth tests. The results given in figure 7 show the evolution of the fatigue crack growth rate, $da/dN = C\ (\Delta K)^m$, for both steels, at room temperature. The values of parameters C and m are shown in table 2.

Thermomechanical approach

The damage of the roll surfaces is also simulated by a thermomechanical fatigue test. This test allows us to study the cyclic behaviour of materials under temperature and stress cycles calculated on the surface of the rolls. Initially, a finite element elastoplastic model was used to evaluate stresses and strains from the temperature distribution. To apply this model, isothermal cyclic characteristics of the material have been experimentally determined.

Method. The particular shape of a roll leads to a plane strain analysis. A middle cross-section of the roll was therefore considered and assumed to be fixed for numerical convenience, whereas, the thermal loading was assumed to rotate.

The finite element analysis, figure 8, was conducted with an elastoplastic model (2) using the following hypothesis :

- Young's modulus and Poisson's ratio are supposed to be independent of the temperature (only because of the computer's capacity) ;
- the yield stress depends on the temperature ;

- there is a linear, kinematic hardening with a temperature dependent coefficient ;

- Uniaxial loading curves used to identify the constitutive parameters, are obtained from isothermal stabilized cycles. Steady state is therefore obtained by calculation after one complete loading cycle.

The numerical resolution uses the initial stress method for the thermal and plastic parts of the strain tensor. The non-linear problem is handled with an original algorithm of projection on the convex yield surface (3).

Results. A typical distribution of radial and hoop skin stresses is given on the figure 9 for the steady state : compression under the hot zones and tension elsewhere.

On the surface of the roll, the axial stress σ_z and the hoop stress σ_θ are very close. Yielding therefore occurs for $\sigma_\theta = \sigma_z = \pm\sigma$ yield.

Figure 10 gives the $\sigma - \varepsilon$ loops during a thermal cycle for the axial direction.

Discussion

Honeycomb cracking. The analysis of the formation and development of the thermal cracks shows that :

- honeycomb cracking appears gradually on the surface and propagates in depth for steel A , figure 6a ; on the other hand, steel B shows, after the first cycles, a constant density of cracks, figure 6b ;

- the maximum length of cracks is stabilized after a certain number of cycles; for steel B this stabilization occurs after the first thermal cycles (figure 11).

In other respects, metallographic observations of the surface of cracked samples display the following mechanisms :

- for steel A , thermal crack initiation is enhanced by the specimen surface oxidation, in fact thermal cracks initiate by the cracking of the oxide layer, due to thermal cycling, figure 12a ;

- in steel B , this phenomenon was not observed ; in this case, crack initiation occurs generally on coarse cementite particles, figure 12b ; this phenomenon can be explained by the difference of mechanical and thermal properties between matrix and carbides.

The thermal coefficients of both steels being similar, the difference of the materials behaviour must be discussed using the mechanical properties. The thermal fatigue strength is, indeed, characterized by the compression strength at elevated temperatures and by the ductility at room temperature.

Steel A shows a higher ductility compared to steel B , for any temperature ; this difference is displayed by tensile elongation and Manson-Coffin's graphs, figure 3b and 5.

Compression strength at elevated temperatures may be expressed by hardness values. Taking this into account, steel B shows a small difference as compared to steel A , figure 4.

The thermal fatigue behaviour of both steels can, then, be explained as follows :

- steel A , more resistant and principally more ductile, shows a higher thermal fatigue strength ; in this case, the mechanism of crack initiation due to thermal solicitations is slow enough to allow the influence of specimen surface oxidation. The crack density increases inside and on the surface of the sample, in relation to thermal cycles and the oxide layer cracking ;

- steel B , less resistant and particularly brittle, shows a poor fatigue strength ; in thermal fatigue, cracks appear during the first cycles. The non-evolution of the honeycomb cracking shows that, immediately after initiation, the thermal cracks grow rapidly by low-cycle fatigue at the matrix-carbide interfaces ;

- the difference in maximum crack lengths between steel A and steel B can be understood by the differences in low-cycle fatigue strength, figure 5.

Crack growth. The acceleration of crack propagation expressed by exponent m , is higher for steel B ($m = 5.5$) than for steel A ($m = 3.4$). These values confirm the proposed relation (4) between the exponent m and the cyclic strain hardening coefficient n'. Table 2 shows that the ratio obtained for steels A and B are in good agreement with the earlier proposed value of this ratio ($m/n' = 20$). In other respects, da/dN-ΔK curves intersect between 10^{-8} and 10^{-7} mm/cycle. Therefore, for $\Delta K < 18$ MPa $\sqrt{m}$, da/dN is higher for steel A than for steel B , whereas for $\Delta K > 18$ MPa $\sqrt{m}$ it is the contrary.

A fractographic analysis of both materials shows :

- steel A reveals at low ΔK a mixed intergranular and transgranular fracture mode, figure 13a, and at high ΔK levels a "brittle striations" appearance, figure 13b. The observation of intergranular fracture zones at low ΔK can not be related to the stress-corrosion susceptibility of the steel ($K_{Iscc} > 46$ MPa $\sqrt{m}$). However two mechanisms may be advanced to explain the grain boundary brittleness :

  . a hydrogen ion diffusion enhanced by high local partial pressures due to a crack tip closure phenomenon ; this phenomenon is displayed by the evidence of an oxyde layer (5) ;

  . a hydrogen ion transport into the lattice by dislocation "sweep-in" (6) ;

- steel B shows a fracture surface corresponding to a ductile matrix and carbides. Carbides are either sheared or uprooted as a fonction of ΔK levels. At low ΔK, carbides are most generally sheared, figure 13c, while for high ΔK there is an increase of roughness of the fracture surface, figure 13d. The increase in roughness can be related to the increase of plastic strain around carbides. In fact, the mechanism of shearing, produced during the loading cycles, by dislocations pile-up at the matrix-carbide interface, leads to lower rates compared with those of steel A .

  On the other hand, the uprooting phenomenon in the highly deformed matrix leads to the assumption that there is a coalescence from one carbide to another, thus enhancing cracking. This phenomenon observed during the tests, can explain the high crack growth rate for a high ΔK range.

REFERENCES

1. Dias, A., and Lieurade, H.-P., 21èmes Journées des Aciers Spéciaux, Saint-Etienne, 27-28 April 1982

2. Giusti, J., 1981, Contraintes et déformations résiduelles d'origine thermique, Thèse, Paris.

3. Nguyen, Q.S., 1973, Contribution à la théorie macroscopique de l'élastoplasticité avec écrouissage, Thèse, Paris.

4. Lieurade, H.-P., 1978, Comportement mécanique et métallurgique des aciers dans le domaine de la fatigue oligocyclique, Thèse, Paris.

5. Bignonnet, A., Namdar-Irani, R., Truchon, M., ECF4, Leoben, 22-24 Sept.1982

6. Tien, J.K., Richards, R.J., Buck, O., Marcus, H.L., 1975, Scripta Met., 9, 1097.

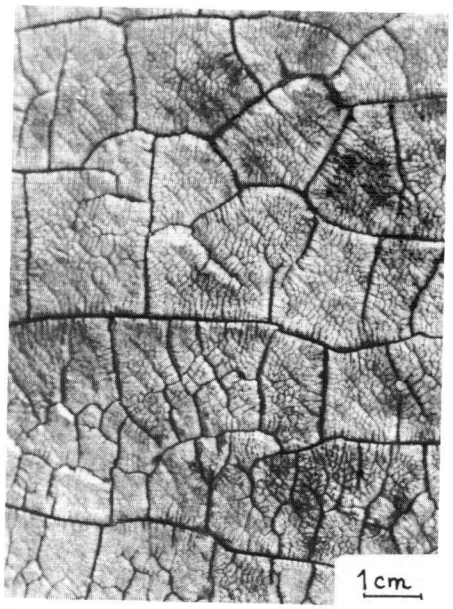

Figure 1 Honeycomb cracking.

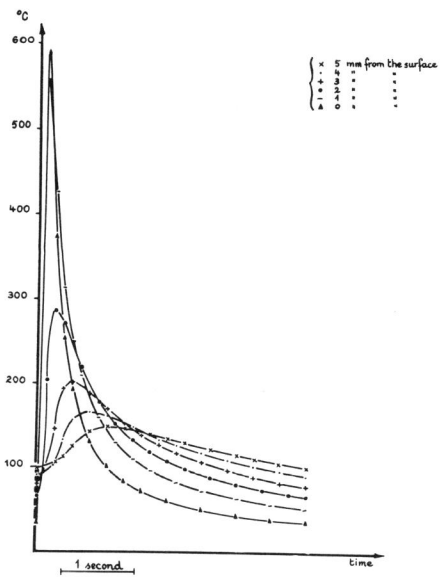

Figure 2 Variation of temperature at roll surface (calculated).

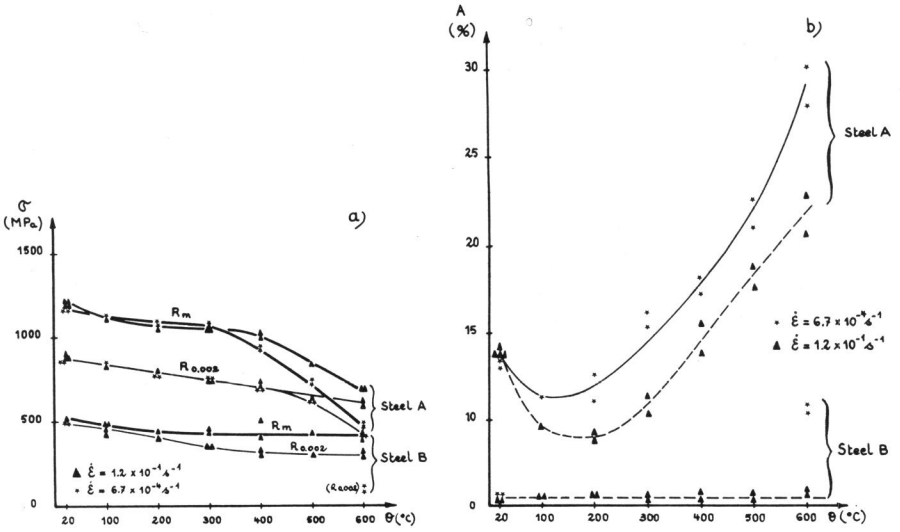

Figure 3 Tensile properties.

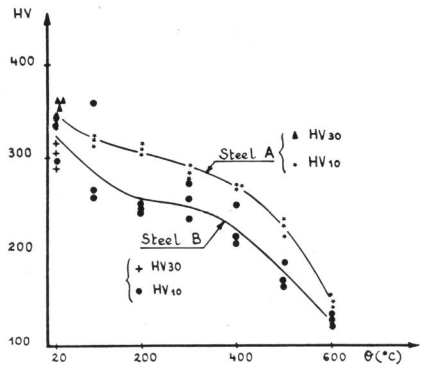

Figure 4 Evolution of the hardness with the temperature.

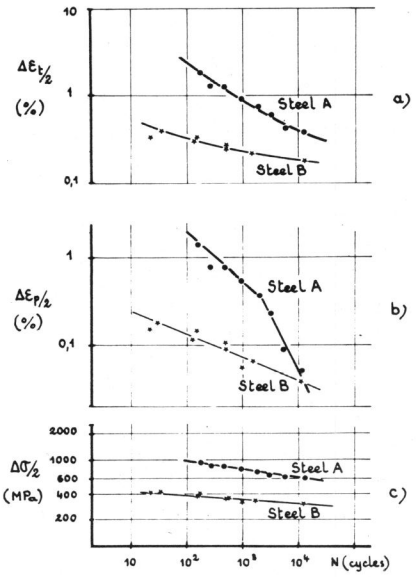

Figure 5 Low-cycle fatigue data, at room temperature.

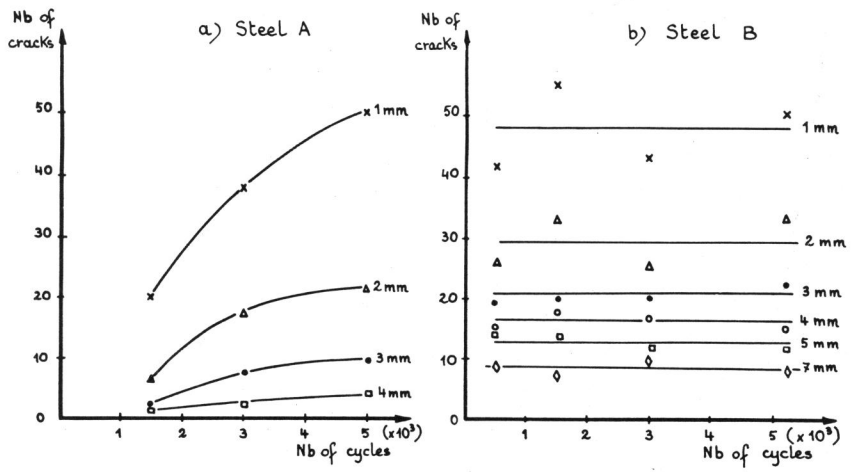

Figure 6 Crack density plotted against the number of cycles.

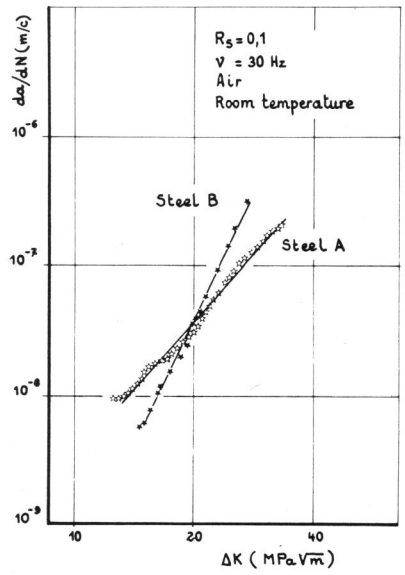

Figure 7 Fatigue crack propagation rates.

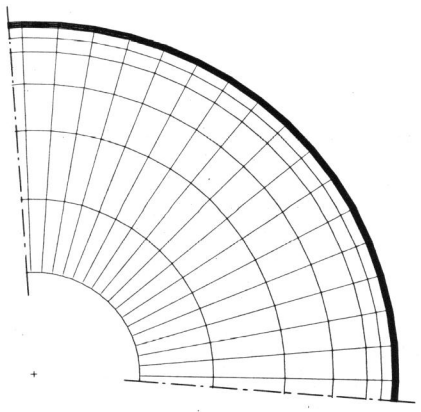

Figure 8 Partial finite element mesh.

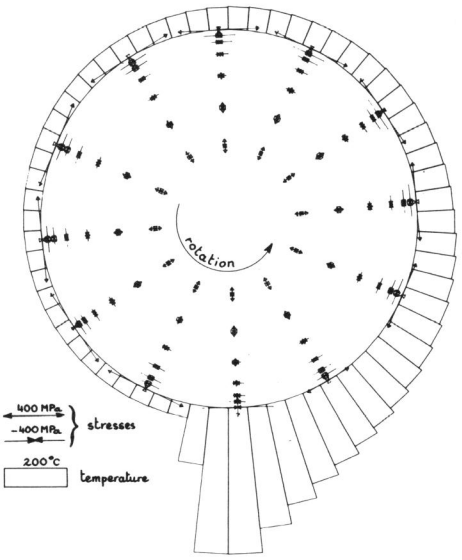

Figure 9 Surface temperature and stresses map during roll rotation

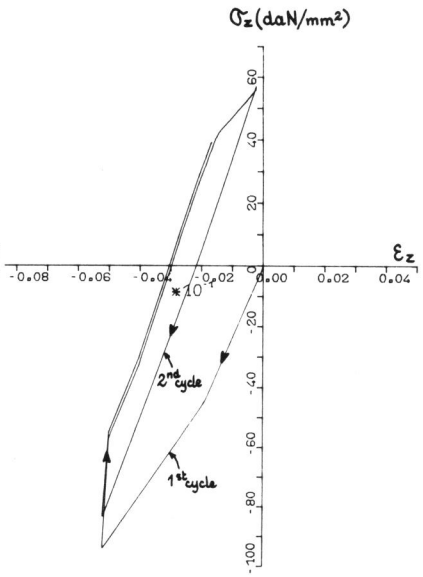

Figure 10 Longitudinal stress-strain loop (calculated).

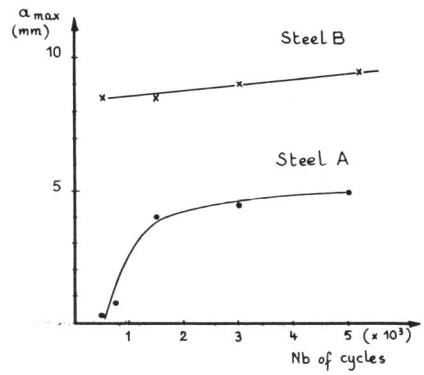

Figure 11 Maximum crack length versus the number of cycles.

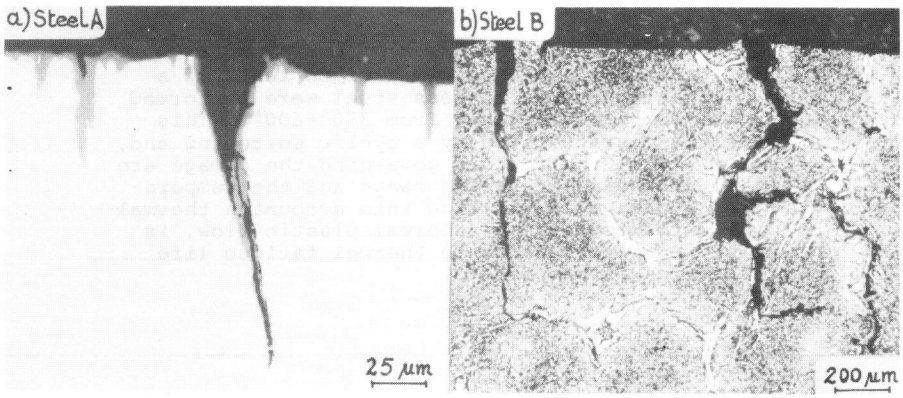

Figure 12 Thermal fatigue crack initiation appearance.

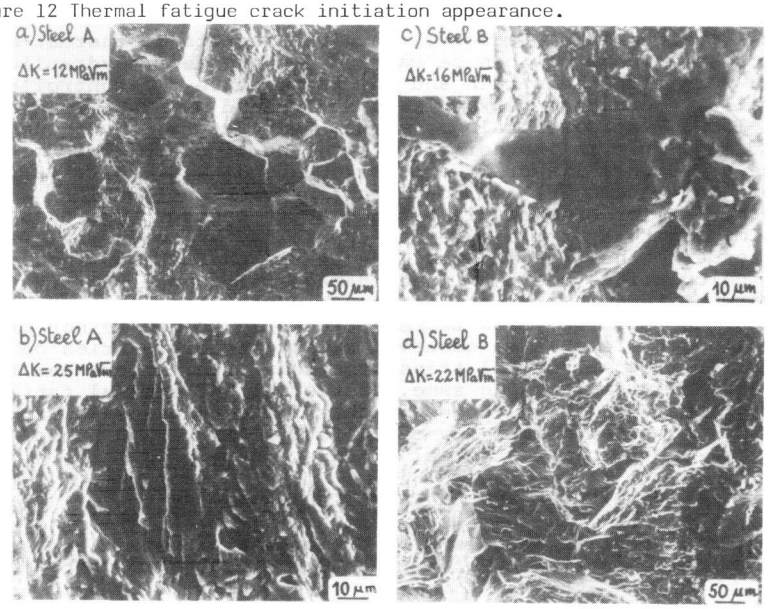

Figure 13 Observations of the fatigue surfaces.